An RF phased array applicator designed for hyperthermia breast cancer treatments

Liyong Wu[1], **Robert J McGough**[1], **Omar Ali Arabe**[2], and **Thaddeus V Samulski**[2]

1*Department of Electrical and Computer Engineering, Michigan State University, East Lansing, MI 48824, USA*

2*Department of Radiation Oncology, Duke University Medical Center, Durham, NC 27710, USA*

Abstract

An RF phased array applicator has been constructed for hyperthermia treatments in the intact breast. This RF phased array consists of four antennas mounted on a Lexan water tank, and geometric focusing is employed so that each antenna points in the direction of the intended target. The operating frequency for this phased array is 140 MHz. The RF array has been characterized both by electric field measurements in a water tank and by electric field simulations using the finite-element method. The finite-element simulations are performed with HFSS software, where the mesh defined for finite-element calculations includes the geometry of the tank enclosure and four end-loaded dipole antennas. The material properties of the water tank enclosure and the antennas are also included in each simulation. The results of the finite-element simulations are compared to the measured values for this configuration, and the results, which include the effects of amplitude shading and phase shifting, show that the electric field predicted by finite-element simulations is similar to the measured field. Simulations also show that the contributions from standing waves are significant, which is consistent with measurement results. Simulated electric field and bio-heat transfer results are also computed within a simple 3D breast model. Temperature simulations show that, although peak temperatures are generated outside the simulated tumour target, this RF phased array applicator is an effective device for regional hyperthermia in the intact breast.

1. Introduction

Among women living in the United States, breast cancer is the most common malignancy diagnosed and the second leading cause of death from cancer (Greenlee *et al* 2000). According to the World Health Organization (http://www.who.int), 1.2 million women worldwide and 274 380 women in the United States were diagnosed with breast cancer in 2004, and the National Cancer Institute (http://www.nci.nih.gov/) predicts that 13.4% of women born today will be diagnosed with breast cancer during their lifetime. Of all women diagnosed with breast cancer, 20% have locally advanced disease (Perez *et al* 1994). Women with locally advanced breast cancer (LABC) who are exposed to standard treatments experience a 5 year survival rate of 50%, and this rate declines to 30% after 10 years (Hortobagyi 1990).

Hyperthermia is a viable treatment option for patients with locally advanced breast cancer. Hyperthermia cancer therapy exposes tumour tissues to elevated temperatures (Wust *et al* 2002, van der Zee 2002, Hildebrandt *et al* 2002) for an extended period of time, where a typical treatment lasts approximately 60 min. Hyperthermia, as applied in the human clinic, artificially increases tumour temperatures to a peak value that is usually between 40 °C and 43 °C

(Hildebrandt *et al* 2002). Research has shown that high temperatures can damage and kill cancer cells with minimal injury to normal tissues (van der Zee 2002).

External heating devices appropriate for deep hyperthermia in the intact breast include ultrasound phased arrays (Hynynen *et al* 2001) and radio-frequency (RF) electromagnetic phased arrays (Zhang *et al* 1993, Fujita *et al* 1993, Kato and Ishida 1993, Gromoll *et al* 2000). Ultrasound is a local modality for heating small targets in the breast (up to about 2 cm diameter (Malinen *et al* 2004)), whereas heat generated by RF electromagnetic devices is delivered regionally across a much larger area. RF phased arrays have been developed previously for deep hyperthermia in the pelvis (Wust *et al* 1991) and in the extremities (Zhang *et al* 1993, Turner 1986), respectively. These arrays apply RF frequencies in the 60–140 MHz range for increased penetration while delivering heat to deep targets. A microwave phased array system has also been constructed for thermal therapy in the breast (Fenn *et al* 1999). The microwave phased array system requires breast compression because of the shallow penetration achieved at 915 MHz.

To exploit the greater penetration depths afforded by RF applicators, a four-channel RF phased array applicator has been developed for hyperthermia cancer treatments in the intact breast. This phased array operates at 140 MHz, which increases the penetration depth substantially over that achieved by microwaves. This RF phased array has been characterized with measurements of the electric field, and these measurements are consistent with the fields predicted by finite-element simulations. Additional finite-element and bio-heat transfer modelling results suggest that this array is capable of delivering therapeutic heat in an idealized model of the breast. These measurement and simulation results show that this RF phased array system can focus the electric field within a water tank and in simulated tumour targets in the breast.

2. RF phased array applicator and *E*-field measurement system

2.1. Applicator geometry

A photograph of the prototype four-antenna RF phased array applicator is shown in figure 1 (a). This design is an adaptation of previous cylindrical phased array geometries (Zhang *et al* 1993, Turner 1984), where only the portion of the array that directs RF energy to the breast is retained. The applicator consists of a water tank enclosure with four pairs of end-loaded dipole antennas mounted on the inner surface of the water tank. The tank enclosure consists of six solid Lexan (GE Polymerland, North America: www.gepolymerland.com) side panels and a Lexan top piece with a large opening. RF antennas are mounted on four of the rectangular side panels, and the two remaining side panels are irregular pentagons with one axis of symmetry. The four rectangular side panels are 12.8 cm by 21.5 cm, and the pentagonal side panels are 12.8 cm by 12.8 cm by 12.8 cm by 12.8 cm by 33.2 cm. In each pentagonal side panel, the obtuse angle measured at the lowest point on the tank is 112°, the two obtuse angles measured at adjacent vertices are 153°, and the two remaining acute angles are 61°. Each Lexan panel is approximately 5 mm thick. The top opening is 33.2 cm by 20.5 cm, the overall size of the tank enclosure in the *x, y* and *z* directions is 21.5 cm by 33.8 cm by 18.4 cm, respectively. For electric field measurements and patient treatments, the water tank is filled with deionized water.

The RF phased array applicator consists of four end-loaded dipole antennas that are composed of attached segments of 0.03 mm thick copper foil (Zhang *et al* 1993). This antenna geometry forms a transmission line with the two horizontal segments, and these in turn guide the RF energy to the vertical sections. For each of the antennas shown in figure 1, the RF voltage input is applied at the centre of the end-loaded dipole. Impedance matching is implemented with a coaxial cable stub, so each antenna is driven at 140 MHz with a low return loss.

2.2. Amplifier system

The main components of the RF phased array amplifier system include a signal generator, a vector voltmeter, a multiplexer, a switch box and four RF power amplifiers (figure 2). The signal source for all channels is an HP (Palo Alto, CA) 8647A signal generator. An HP (Palo Alto, CA) 8508A vector voltmeter measures the output phase and power as well as the reflected power. These measurements deliver phase and power feedback to the controlling computer via GPIB. The multiplexer/switch box combination specifies the amplitude and phase of the input to the RF power amplifiers with analogue attenuators and phase shifters through a Kontron (San Diego, CA) AOB6-P digital-to-analogue converter (DAC) card that is installed in the controlling computer. The RF power amplifiers are LCF Enterprises (Post Falls, ID) model B020 rack-mount amplifier systems that operate in the 120–170 MHz frequency range with a maximum power output of 150 W. The output of each RF power amplifier is attached to a circulator, a low-pass filter, and a directional coupler that provides a direct connection to the antenna and a feedback connection to the vector voltmeter. The controlling computer is a Pentium II system with 128 MB of RAM running the Windows 98 operating system, and the system control software is written in Visual Basic (Microsoft Corporation; Redmond, WA).

2.3. Measurement system

The electric field is measured with an *E*-field probe attached to a three-axis positioning system. The measurement system hardware consists of (1) a LinTech (Monrovia, CA) M1-102412 three-axis positioning system, (2) three EP-400 *E*-field array probes from BSD Medical Corporation (Salt Lake City, UT), (3) an HP/Agilent (Palo Alto, CA) 34970A Data Acquisition/ Switch Unit, (4) three Digiplan (Poole, Dorset, UK) PDX15 motor drivers (one for each axis), (5) a custom water degasser and (6) a personal computer (PC). The *E*-field mapping software is controlled through a Matlab graphical user interface operating on a Windows 98 platform. Low-level interface routines are provided by the Matlab Instrument Control toolbox. The EP-400 *E*-field probes are connected to the HP 34970A, which transfers measured voltage values to the PC via GPIB. The stepper motor positioning system is controlled by the Digiplan motor drivers, and these communicate with the PC through a daisy-chained serial port connection.

The three-axis probe combines three separate EP-400 *E*-field array probes attached to a Plexiglas rod in the orthogonal arrangement shown in figure 3. Each probe contains three miniature diodes, so the three-axis *E*-field probe consists of nine miniature diodes. This arrangement permits averaging of the individual *E*-field components, which improves the signal-to-noise ratio for each *E*-field measurement. Each probe is offset from the centre of the Plexiglas rod, and the control software compensates for the offset distance before the signals are averaged.

3. Simulation methods

3.1. Electric field computations with the finite-element method

Most computations of the electric field (*E*-field) generated by radio-frequency (RF) electromagnetic devices designed for hyperthermia presently utilize either the finite difference time domain (FDTD) method (Sullivan *et al* 1987) or the finite-element method (FEM) (Paulsen *et al* 1993, Clegg *et al* 1996, Kumaradas and Sherar 2003). The finite-element method provides an advantage in *E*-field modelling by facilitating the geometric adaptability of the computational mesh. The finite-element method solves the weak form of the vector wave equation (Jin 2002)

$$\int_V \left[\frac{1}{\mu_r} (\nabla \times \mathbf{E}) \cdot (\nabla \times \mathbf{W}) - k_0^2 \varepsilon_r \mathbf{E} \cdot \mathbf{W} \right] \mathrm{d}V = - \int_{s_0} \mathbf{W} \cdot (\hat{n} \times \nabla \times \mathbf{E}) \, \mathrm{d}S - \int_V \mathbf{f} \cdot \mathbf{W} \, \mathrm{d}V.$$

(1)

This expression describes the *E*-field throughout the volume *V* subject to a given set of boundary conditions on the surface S_0 enclosing the volume *V*. In equation (1), μ_r is the relative permeability, **W** is a weighting function, ε_r is the relative permittivity, k_0 is the wavenumber in free space, and **f** is the electromagnetic source function given by

$$\mathbf{f}=jk_0 Z_0 \mathbf{J} + \nabla \times \left(\frac{1}{\mu_r}\right)\mathbf{M}.$$

(2)

In equation (2), Z_0 is the free space wave impedance, **J** is the electric current density, and **M** is the magnetic current density. The first item on the right-hand side (RHS) of equation (1) is the boundary integral, which vanishes on a perfect electrical conductor (PEC) and represents the absorbing boundary condition on a truncated surface for an open structure (Jin 2002).

Finite-element simulation results are generated by HFSS Version 8.0, which is a commercial software package produced by Ansoft Corp. (Pittsburgh, PA). In HFSS simulations of the electric field generated by the phased array applicator, the computational model consists of a three-dimensional mesh of tetrahedral elements. HFSS provides a convenient interface for defining geometric structures and assigning material properties of each structure, then HFSS automates the generation of the mesh based on the structural properties of the overall system. In each tetrahedral element, the initial lengths of the edges are determined from the material properties, and the mesh is automatically refined on the basis of the results of the computed *E*-field. The convenient user interface provided by HFSS allows an experienced operator to quickly define a new applicator structure and phantom geometry, generate the corresponding mesh, and solve for the resulting *E*-fields.

Finite-element simulations of the phased array applicator truncate the boundary of the defined mesh with an absorbing boundary condition (ABC). The ABC for these simulations is implemented as a second-order radiation boundary condition located in the air surrounding the outside the applicator. In HFSS, the ABC elements are cuboids that surround the computational volume. The absorbing boundary is located roughly $\lambda/10$ away from the applicator, and since the antennas radiate primarily into the water tank, the *E*-field decays significantly before reaching the ABC. Results (not shown) were also obtained with an absorbing boundary located λ from the applicator. The difference between the computed fields obtained with the boundaries at $\lambda/10$ and λ is approximately 1.24%; therefore, the distance from the water tank to the absorbing boundary is $\lambda/10$ for all simulations. By placing the ABC closer to the applicator, the size of the mesh is reduced, which in turn diminishes the computer memory requirements and the total computation time.

The *E*-field distribution is computed for each antenna separately, and then the results are superposed. The magnitude of the total *E*-field is computed according to

$$|\mathbf{E}(x,y,z)| = |\sum_{n=1}^{N} \mathbf{U}_n(x,y,z)\, I_n|,$$

(3)

where I_n is a complex number representing the amplitude and the phase of the *n*th antenna input, and the vector **I** steers and focuses the *E*-field. In equation (3), $\mathbf{U}_n$ represents the electric field contribution produced by the *n*th antenna for a unit input excitation (i.e., $I_n = 1\angle 0°$), $N = 4$ is the number of the antennas in the phased array applicator, **E** represents the total electric field, and (*x, y, z*) represents the Cartesian coordinates of the simulated *E*-field. In the simulation model, the voltage excitation is located at the centre of the antenna, and each antenna input is modelled as a lumped gap source located at the centre of each input port with an impedance of 50 Ω. Once the 3D *E*-field is computed, the SAR is calculated from the amplitude of the total *E*-field according to

$$\mathrm{SAR}\,(x,y,z) = \frac{\sigma\,(x,y,z)}{2\rho\,(x,y,z)}\,|\mathbf{E}\,(x,y,z)\,|^2,$$

<div align="right">(4)</div>

where σ represents the conductivity and ρ represents the density for each tissue type.

3.2. Geometric models

Figure 4 contains a geometric description of the simulation model for the four-antenna phased array applicator. In the finite-element model, the size of the Lexan tank matches the dimensions of the prototype applicator. The Lexan tank is surrounded by air and filled with deionized water. In these simulations, the relative permittivity of Lexan is $\varepsilon_r = 2.9$, the conductivity of Lexan is $\sigma = 0$, the relative permittivity of deionized water is $\varepsilon_r = 76.5$, and the conductivity of deionized water is $\sigma = 0.0001$ S m^{-1}. The four end-loaded dipole antennas, which are attached to the Lexan tank, are copper strips excited by a lumped gap source. The resulting E-field is evaluated in the water tank and in a tissue phantom model suspended within the water tank.

The simulated tissue phantom in these finite-element simulations is the simplified 3D breast model shown in figure 5. This 3D model, which was in part motivated by the axi-asymmetric model in Paulsen *et al* (1984), consists of an extended hemisphere and a spherical tumour mass that is offset somewhat with respect to the central axis of the breast model. The model in figure 5 includes a skin layer, a fat layer and a muscle layer. In figure 5, the radius of the hemispherical breast is 7.5 cm, the radius of the simulated tumour mass is 2.5 cm, the thickness of the skin layer is 0.5 cm, the muscle layer is about 4.2 cm thick, and the fat layer is 1 cm thick. In this model, skin, breast and fat share the same material property values (Paulsen *et al* 1988). The material properties for each tissue type are listed in table 1. In the FEM simulations, the applicator in figure 4 is filled with deionized water, and the breast model is suspended in deionized water. The E-field is then computed in the breast and all surrounding regions, including the deionized water, the Lexan tank and the surrounding air space.

3.3. Bio-heat transfer model

The temperature distribution is determined from the computed SAR distribution using the steady-state bio-heat transfer equation (BHTE) (Roemer *et al* 1984),

$$0 = \kappa\nabla^2 T + c_b W_b\,(T - T_b) + \sigma\,|\mathbf{E}\,|^2.$$

<div align="right">(5)</div>

In equation (5), κ is the thermal conductivity (W m^{-1} $^\circ$C^{-1}), T is the tissue temperature ($^\circ$C), c_b is the specific heat of blood (J kg^{-1} $^\circ$C^{-1}), W_b is the blood perfusion rate (kg m^{-3} s^{-1}), T_b is the temperature of blood ($^\circ$C), σ is the electrical conductivity, and $|\mathbf{E}|^2$ is the square of the magnitude of the electric field. In these simulations, the steady-state finite difference solution of equation (5) is obtained for the resulting tissue temperature T. The finite difference calculations maintain the water surrounding the breast at a constant temperature, and a radiation boundary condition is enforced at the remaining interfaces. Subject to these boundary conditions, the finite difference model is evaluated within a computational grid that contains the entire 3D model of the breast depicted in figure 5. The grid elements are cuboids, and each grid location contains SAR values obtained from the truncated finite-element mesh defined for E-field calculations.

3.4. Focusing strategy

After FEM calculations of the electric field are obtained for each of the individual antennas, the phased array is then focused in the water tank and in a simulated breast phantom. The E-field is typically focused by optimizing the SAR (Kroeze *et al* 2001, Das *et al* 1999a, Wiersma *et al* 2002, van Rhoon *et al* 2003), and focusing is also achieved by directly optimizing the

temperature (Das *et al* 1999b). Here, the phased array is focused by maximizing the constructive interference produced by the individual *E*-field components at a single point. A focus is generated when the magnitude squared of the total *E*-field

$$|\mathbf{E}|^2 = \sum_{m=1}^{4} \sum_{n=1}^{4} (U_m I_m)(U_n I_n)^*$$

(6)

is maximized relative to the sum of the squared input magnitudes $\sum_{n=1}^{4} |I_n|^2$. Defining the individual components of **E** through a matrix–vector product yields (Das *et al* 1999b)

$$\begin{bmatrix} E^X \\ E^Y \\ E^Z \end{bmatrix} = \begin{bmatrix} U_1^X & U_2^X & U_3^X & U_4^X \\ U_1^Y & U_2^Y & U_3^Y & U_4^Y \\ U_1^Z & U_2^Z & U_3^Z & U_4^Z \end{bmatrix} \begin{bmatrix} I_1 \\ I_2 \\ I_3 \\ I_4 \end{bmatrix},$$

(7)

which is equivalent to $\underline{\mathbf{E}} = \underline{\underline{\mathbf{U}}}\,\underline{\mathbf{I}}$, where a single underbar indicates a vector quantity and a double underbar indicates a matrix quantity. After this matrix–vector notation is applied to equation (6) and the result is normalized with respect to the sum of the squared input magnitudes $\langle \underline{\mathbf{I}}, \underline{\mathbf{I}} \rangle = \underline{\mathbf{I}}^{*t}\underline{\mathbf{I}}$, the optimization problem becomes

$$\max_{\underline{\mathbf{I}}} \frac{\langle \underline{\mathbf{E}}, \underline{\mathbf{E}} \rangle}{\langle \underline{\mathbf{I}}, \underline{\mathbf{I}} \rangle} = \max_{\underline{\mathbf{I}}} \frac{\underline{\mathbf{I}}^{*t}\underline{\underline{\mathbf{U}}}^{*t}\underline{\underline{\mathbf{U}}}\,\underline{\mathbf{I}}}{\underline{\mathbf{I}}^{*t}\underline{\mathbf{I}}}.$$

(8)

The extrema of the quadratic form in equation (8) are the eigenvalues of $\underline{\underline{\mathbf{U}}}^{*t}\underline{\underline{\mathbf{U}}}$, and the maximum value λ_{max} of equation (8) is achieved by the eigenvector $\underline{\mathbf{I}}_{max}$ of $\underline{\underline{\mathbf{U}}}^{*t}\underline{\underline{\mathbf{U}}}$ (Das *et al* 1999b) that satisfies

$$\underline{\underline{\mathbf{U}}}^{*t}\underline{\underline{\mathbf{U}}}\,\underline{\mathbf{I}}_{max} = \lambda_{max}\underline{\mathbf{I}}_{max}.$$

(9)

The input $\underline{\mathbf{I}}_{max}$ maximizes the power deposition at a single coordinate in the tumour target. As a result, constructive interference is also achieved in nearby regions, and the surrounding tumour tissue is also heated. The optimal excitation vector $\underline{\mathbf{I}}_{max}$ is selected such that the peak power deposition is located within the tumour in a location proximal to the applicator. Focusing in this location reduces hot spots in normal tissues and other problems related to penetration depth.

The expression in equation (9) represents the optimal solution when the magnitudes and phases of the excitation are unconstrained. If the magnitudes of the entries in $\underline{\mathbf{I}}$ are specified in advance, then the expression in equation (6) is a nonlinear function of the phase variables $\arg(I_n) = \phi_n$. Defining the arguments of the antenna outputs for unit input excitations as $\arg(U_m^X) = \theta_m^X, \arg(U_m^Y) = \theta_m^Y$ and $\arg(U_m^Z) = \theta_m^Z$ yields an equivalent objective function

$$\sum_{n=1}^{2} \sum_{m=n+1}^{3} |I_n||I_m| \left\{ |U_n^X||U_m^X|\cos\left(\theta_n^X + \theta_m^X + \phi_n - \phi_m\right) \right.$$
$$+ |U_n^Y||U_m^Y|\cos\left(\theta_n^Y - \theta_m^Y + \phi_n - \phi_m\right) + |U_n^Z||U_m^Z|\cos\left(\theta_n^Z - \theta_m^Z + \phi_n - \phi_m\right) \right\}$$
$$+ \sum_{n=1}^{3} |I_n||I_4| \left\{ |U_n^X||U_4^X|\cos\left(\theta_n^X - \theta_4^X + \phi_n\right) \right.$$
$$+ |U_n^Y||U_4^Y|\cos\left(\theta_n^Y - \theta_4^Y + \phi_n\right) + |U_n^Z||U_4^Z|\cos\left(\theta_n^Z - \theta_4^Z + \phi_n\right) \right\}$$

(10)

when the reference phase for the fourth input is $\phi_4 = 0°$. The expression in equation (10) is readily maximized by iterative solvers such as the Matlab function *fminunc,* which quickly converges to the optimal values of ϕ_1, ϕ_2 and ϕ_3 that produce a global maximum. Solutions to

both the linear and nonlinear objective functions in equation (9) and equation (10), respectively, generate viable focal patterns for thermal therapy.

4. Results

4.1. E-field measurements in the water tank

The electric field is focused in the water tank with an appropriate selection of phases and amplitudes. A focus is generated by iteratively modifying the phase, and the combination of phase values that produce the maximum peak magnitude of the measured electric field in the desired location is selected as the input. This focusing approach is required because of the phase errors that are typically present in RF phased array systems (Straube *et al* 1995, Hornsleth *et al* 1997, Lamprecht *et al* 2000). These phase errors are in part caused by the unavoidable crosstalk between antennas that are coupled to a resonant cavity (the water tank) filled with low-loss material (deionized water) and in part caused by errors inherent in the controlling hardware (Straube *et al* 1995, Hornsleth *et al* 1997, Lamprecht *et al* 2000). After the desired combination of input phases and amplitudes is determined, the resulting *E*-field distribution is measured with the *E*-field probe depicted in figure 3.

A focus was achieved at the centre of the water tank with input phase settings of $0°$, $-60°$, $-30°$ and $-90°$ applied to channels 1, 2, 3 and 4, respectively. Forward power settings of 40W were applied to each channel, and for the centred focus, the measured values of the reflected powers were 3.4 W, 3.9 W, 10.4 W and 1.7 W for channels 1, 2, 3 and 4, respectively. The measured *E*-field distribution for the centred focus is shown in figure 6. In each figure, the total *E*-field is the square root of the sum of the squares of the individual component magnitudes. The measured *E*-field values in figure 6 are indicated by a star ('*') symbol, and the intermediate values indicated by dashed lines are obtained from the results of cubic spline interpolation. Figure 6(a) contains the measured *E*-field along the *x*-axis, figure 6(b) shows the measured *E*-field along the *y*-axis, and figure 6(c) demonstrates the measured *E*-field along the *z*-axis. Figures 6(a) and (b) show that the desired peak is located near the centre of the water tank. Figure 6(c) indicates that the maximum measured value along the *z*-axis is located 3 cm below the water surface and the minimum measured value is located 12 cm below the water surface.

A steered focus was generated in the water tank with input power values of 50 W for channels 1 and 2 and 25W for channels 3 and 4. The phase settings for the steered focus were $0°$, $0°$, $-130°$ and $-130°$ and the measured reflected powers were 65W, 9W, 0.4 W and 14 W for channels 1, 2, 3 and 4, respectively. These reflected power values emphasize the need for circulators in the amplifier system while indicating that focusing is preferentially achieved at the centre of the water tank. The measured *E*-field distribution is shown in figure 7(a), which shows that the peak is located at $(0, 4, -3)$ cm.

4.2. E-field simulations in the water tank

Simulation results for specified input settings are obtained by superposing the contributions from each antenna. In these simulations, the *E*-field is computed separately for each antenna using a common finite-element mesh. This mesh is defined by the model geometry and the material properties of water, Lexan, copper and air, and for the breast model, material properties of different tissue types are also included. The finite-element mesh is initially generated by HFSS and then automatically refined. Additional manual mesh refinement is applied as necessary near material interfaces, in regions where the electric field is changing rapidly, and in regions where node spacings are otherwise too large. After the mesh generation is completed, the average distance between adjacent nodes is between $\lambda/10$ and $\lambda/75$, depending on the model geometry and material properties, with higher node densities near radiating sources and material interfaces. The finite-element mesh includes an absorbing boundary condition, where

the shortest distance in air from the edge of the water tank to the absorbing boundary is 20 cm in the *x*-direction, 18 cm in the *y*-direction, 20 cm measured from the top of the water tank in the *z*-direction, and 12 cm measured from the bottom of the water tank in the *z*-direction.

A typical finite-element simulation consists of an initial automated mesh generation, 11 automated mesh refinements, and one or more additional manual refinements resulting in a mesh containing up to 73 000 tetrahedra. After each mesh refinement, the *E*-field is computed with the finite-element method using an edge element formulation. The computation time associated with this sequence of calculations is about 8 h on a 2.4 GHz Pentium 4 personal computer with 1 GB RAM running the Windows XP operating system.

A simulated focus at the centre of the water tank is generated with uniform power and phase inputs. The simulated inputs are normalized with respect to the peak input power, so the input power applied to each channel is 1 W, and the phase value is 0° for each input channel. The simulated *E*-field distribution for the centred focus is shown in figure 6. Each plot is also normalized, which facilitates comparisons between simulated and measured values. The simulated *E*-field values in figure 6 are indicated by solid lines, where figure 6(a) contains the simulated *E*-field along the *x*-axis, figure 6(b) shows the simulated *E*-field along the *y*-axis, and figure 6(c) demonstrates the simulated *E*-field along the *z*-axis. Figures 6(a) and (b) show that the simulated peak is again near the centre of the water tank. Figure 6(c) indicates that the simulated peak value along the *z*-axis is also located about 3 cm below the water surface.

The simulated focus is steered to the right with input powers of 0.5W, 0.5W, 1 W and 1W and input phases of −87°, −91°, −66° and 0° applied to channels 1, 2, 3 and 4, respectively. The input power values in these simulations are proportional to the input powers that generated the measured *E*-field distribution depicted in figure 7(a), and the input phases maximize the objective function in equation (10) for a focus selected at (0, 4, −3) cm. This target represents the location of the peak *E*-field magnitude and the maximum constructive interference. The phases that generate this result were obtained from the solution to equation (10), which converged to the optimal solution after 170 iterations.

4.3. Breast model simulations

Simulations that combine the applicator model in figure 4 with the breast tumour model in figure 5 demonstrate an example of RF energy focused within a tumour target. In these simulations, the breast model is suspended in the water tank such that the skin layer indicated in figure 5 is parallel to the flange on the top of the water tank, and then the breast model is centred within the opening on top of the tank. The *E*-field is focused on the tumour in the breast model with the solution to the eigenvalue problem in equation (9), and the resulting *E*-field, SAR, and temperature response are computed in 3D using the material properties in table 1. The ABC boundaries for the breast model are the same as those defined earlier for *E*-field simulations in the water tank. These dimensions encompass the simulation model that combines the applicator in figure 4 and the breast tumour model in figure 5. After the *E*-field is computed, the SAR is calculated with equation (4). To reduce the memory and time required for temperature calculations, SAR values are stored within a restricted volume that contains the entire breast and some connected soft tissues. For SAR and temperature calculations only, the *x* values are limited to the range from −81 mm to 81 mm, the *y* values are limited to the range from −81 mm to 81 mm, and the *z* values are limited to the range from −110 mm to 110 mm. Since there is very little penetration beyond the breast at 140 MHz, the SAR distribution in these restricted coordinates produces approximately the same temperature distribution in the breast as the larger grid of SAR values in much less time. The temperatures in the breast are then calculated with a steady-state finite difference implementation of equation (5) that maintains a boundary condition of 39 °C in the water tank, where this boundary condition simulates the effect of a circulating water bath during a patient treatment.

The results of these E-field, SAR and temperature calculations are shown in figure 8 and figure 9 for a focus located at $(x, y, z) = (0, −15, −67)$ mm, which is within the tumour model near the tumour boundary and proximal to the applicator. The computed values for the E-field, SAR and temperature in figure 8 are demonstrated in the central portion of the breast model evaluated in the $x = 0$ plane. The E-field, SAR and temperature values in figure 9 are evaluated in the $y = −16$ mm plane, where the peak SAR and temperature values occur. This plane is near the centre of the spherical tumour model, which is located at $(x, y, z) = (0, −12, −50)$ mm in the applicator coordinate frame. The centre of the breast is located at $(x, y) = (0, 0)$ mm in this coordinate frame, with the surface of the skin layer defined in figure 5 coincident with the $z = 0$ plane.

The antenna phases that generate these results are $\theta_1 = 26.76°$, $\theta_2 = 72.4°$, $\theta_3 = 60.2°$ and $\theta_4 = 0.0°$, and the corresponding magnitudes of each excitation are $|I_1| = 0.65$, $|I_2| = 1.0$, $|I_3| = 0.85$ and $|I_4| = 0.57$. The E-field and SAR values are scaled such that the peak overall output temperature is equal to 43.6 °C. The computed fields shown in figure 8 and figure 9 are obtained after the scale factor is applied. Figure 8(a) shows that the largest E-field values in water are located near the individual antennas, whereas in tissue, the peak E-field values in the $x = 0$ plane are near the skin surface. In figure 9(a) (which is orthogonal to the result shown in figure 8(a)), the peak E-field values are located near the skin surface and in fat near the tumour interface. The corresponding SAR distributions are depicted in figure 8(b) and figure 9(b). The computed SAR distributions indicate that multiplying the squared E-field by higher values of conductivity in the tumour model shifts the locations of some peaks into the tumour, although significant SAR contributions remain near the skin in figure 8(b) and in fat near the tumour in figure 9(b). Overall, the computed temperatures in figure 8(c) and figure 9(c) follow trends similar to those established for the SAR distributions in figure 8(b) and figure 9(b). In particular, the temperature peak occurs within the tumour model in figure 8(c), and the peak temperatures occur in fat near the tumour interface in figure 9(c). The overall temperature peak is 43.6°C, which is achieved in figure 9(c) at $(x, z) = (−27$ mm$, −62$ mm$)$ and $(x, z) = (27$ mm$, −62$ mm$)$. These simulation results demonstrate an example of the regional heating that is produced by this RF breast applicator. Although a focus is generated within the tumour, boundary conditions and material properties strongly influence the locations of the SAR and temperature peaks.

5. Discussion

5.1. Measured and simulated E-fields in the water tank

Figure 6 and Figure 7 show that finite-element simulations predict the approximate shape and location of the focus generated by the RF phased array applicator. Figures 6(a) and (b) demonstrate that, for a focus at the centre of the water tank, the measured and simulated E-field distributions are closely aligned along the x- and y-axes, respectively, for magnitudes evaluated at $z = −3$ cm. Figure 6(c) also indicates that the finite-element results successfully predict the locations of the minimum and maximum values along the z-axis. Likewise, simulations and measurements indicate that the E-field distributions are also similar for a steered focus as shown in figure 7. These figures demonstrate that the focus generated by this RF phased array is quite broad, which suggests that this device is appropriate for regional heating.

Some differences between the measured and simulated E-field distributions are also evident in these figures. For example, simulated and measured values along the z-axis in figure 6(c) diverge outside the water tank. In particular, the measured E-field drops off rapidly in air beyond the water interface, whereas the simulated E-field decays slowly. Although the simulated E-field is similar to the measured E-field near the focus in figure 7, the differences between simulated and measured E-fields increase with distance from the focal peak.

These differences are attributed to simulation and measurement errors. Finer meshes will reduce the numerical error where the E-field is changing rapidly, and memory limitations also restrict the total number of tetrahedrons in the finite-element mesh. For these simulations of the E-field produced in the water tank, the average distance between adjacent nodes is 0.0306λ in air, 0.0134λ in lexan and 0.05λ in water. Nodes in the finite-element mesh are more closely spaced near interfaces, where the E-field changes rapidly, and where the magnitude of the E-field is relatively large, whereas the distance between adjacent nodes increases where relatively small E-field magnitudes are changing slowly. The error is introduced by the absorbing boundary is relatively small, as indicated by simulations that compare results for absorbing boundaries located $\lambda/10$ and λ from the water tank. Errors in the tank dimensions, antenna dimensions and antenna locations likewise contribute to errors in the numerical model.

Errors are also introduced by misalignment between the simulation model and the measurement grid. Another source of error is the inherent misalignment between the three E-field probes. These E-field probes were applied to each measurement, and then the results were averaged to improve the signal-to-noise ratio. The relative probe locations were carefully measured before and after these measurements; however, probe locations changed after the probes were repeatedly inserted into the water tank and extracted from the water tank. In addition, some coupling between the computer-controlled three-axis positioning system and the RF applicator was observed during these measurements. As a result, the probes were mounted on a polycarbonate rod, which was then attached to the three-axis positioner. Additional shielding was added as necessary. Although this reduced the noise somewhat, the coupling between the applicator and the positioner nevertheless persisted, and this coupling influenced the measurement results.

Coupling between antennas is also evident in these measurements. This coupling is in part caused by standing waves within the water tank. The standing wave pattern changes as the input phases and amplitudes are varied, which also changes the coupling between antennas. The coupling also changes depending on the load in the water tank. In particular, the coupling changes for different water levels and for different phantom materials placed in a plastic cup on the water surface. This coupling is responsible in part for the differences between the measured and simulated phases and amplitude settings required for a focus at the centre of the tank and for a steered focus. These effects, which are commonly encountered in RF phased array systems designed for hyperthermia (Straube *et al* 1995, Hornsleth *et al* 1997, Lamprecht *et al* 2000), are reduced by focusing the breast applicator at the centre of the water tank so that the reflected powers are minimized. This defines the location where preferential focusing is achieved for this RF phased array applicator.

5.2. Focusing strategy

The simulated focus was generated in the water tank and in the breast model with a modified version of an approach that was defined previously for temperature optimization (Das *et al* 1999b). This approach, which is similar to a method that focuses ultrasound therapy arrays (Ebbini and Cain 1989), maximizes the gain from the aperture to the focus. Equation (9) and Equation (10) provide an alternative to more complicated methods that maximize the total SAR in the entire tumour relative to the total SAR generated in normal tissues (Clegg *et al* 1996, Wiersma *et al* 2002, Sullivan 1992). With this simplified focusing approach, the results presented in figure 8 and figure 9 are obtained for a focus that is generated along the edge of the tumour in a location that is proximal to the applicator. This location minimizes the path to the focus through the tumour, thus reducing the effects of penetration depth on the magnitude of the simulated focus. Similar results (not shown) are obtained for this applicator geometry and breast model with the optimization method outlined in Wiersma *et al* (2002). With the

focusing approach of equation (9) and equation (10), additional optimization is facilitated through control of the focus and the total input power.

5.3. Simulated E-fields evaluated in the breast model

The simulation results depicted in figure 8(a) and figure 9(a) show the *E*-field within a restricted field of view for the 3D breast model. Although the *E*-field was computed for a much larger range of coordinate values, the *E*-field results are demonstrated in the restricted field of view for two reasons. First, these results follow the same range of coordinate values shown in figure 8(b) and figure 9(b) for the SAR and in figure 8(c) and figure 9(c) for the temperature. Plotting these results on the same axes promotes comparisons of the similarities and differences between the computed *E*-field, SAR and temperature distributions. Second, restricting the field of view centres attention on the computed *E*-field in soft tissues. Including the fields near the antenna obscures the fine structure of the *E*-field distribution in soft tissues as demonstrated in figure 8(a), where the magnitude of the *E*-field immediately adjacent to the RF antennas is significantly greater than in soft tissue. In planes that avoid the near field of the individual source antennas, more detail is clearly evident, as demonstrated in figure 9(a). This figure, which reduces the dynamic range by roughly a factor of 2 relative to figure 8(a), shows the full range of computed values in the $y = -16$ cm plane. By restricting the range of coordinate values in this plot, the computed values in tumour and fat are emphasized.

For the computed *E*-field evaluated across the entire range of coordinate values (not shown), the largest magnitudes are generated near the antennas, and intermediate values are indicated in water and within the soft tissue target. These simulations also show that the *E*-field decays rapidly in air. This result suggests that the RF phased array applicator operates as a resonant cavity that produces standing waves within the coupling medium. These standing waves, which are manipulated by the phase and amplitude inputs of the RF phased array applicator, produce peaks and valleys as indicated in figure 6. The peaks and valleys produced by the standing wave patterns are manipulated through scanning and focusing, and these standing wave patterns also influence the reflected powers that are measured at the antenna inputs. In order to avoid unfocused near field components, the breast is positioned some distance away from the individual antennas, preferably at or near the geometric focus of the resonant cavity. Although the *E*-field values are relatively small in air, these values also influence the computed field through the boundary conditions. Simulation results (not shown) indicate that the material behind the breast also influences the distribution of the *E*-field in the breast and in the water tank at 140 MHz. This suggests a need for more detailed patient models, which are presently under development for these simulations. The simulation results also depend on the distance between adjacent nodes in the finite-element mesh. In simulations of the *E*-field generated in the breast model, the average distance between adjacent nodes is 0.0466λ in air, 0.0213λ in lexan, 0.0852λ in water, 0.0701λ in fat and 0.0311λ in the simulated tumour. As in previous simulations, the nodes are more closely spaced near interfaces, where the *E*-field changes rapidly, and where the magnitude of the *E*-field is relatively large, and the distance between adjacent nodes increases for relatively small *E*-field magnitudes that are changing slowly.

Figure 8(a) and Figure 9(a) show that peak magnitude of the *E*-field is located outside the tumour boundary, and similar effects are also observed for peak SAR and temperature values. In figure 8(a), the peak magnitude of the *E*-field in water is located near one of the antennas, and the peak magnitude of the *E*-field in soft tissue is located just beneath the skin surface. In figure 9(a), peak *E*-field magnitudes are adjacent to the tumour boundary in fat. Although the constructive interference is maximized at the focus within the tumour, the magnitude of the *E*-field is significantly greater at the peak outside the tumour in figure 9(a). This effect is a consequence of the boundary conditions at the tumour/fat interface and the orientation of the *E*-field generated by the RF phased array applicator. This combination maximizes the *E*-field

outside the tumour model, and a severe impedance mismatch at the boundary reduces the peak magnitude of the *E*-field within the tumour target.

A similar trend is observed for the SAR distribution in each plane. In figure 8(b), the peak SAR value within the tumour is approximately the same as the peak SAR value located just beneath the skin surface. In figure 9(b), the peak SAR within the tumour also approaches the peak SAR achieved along the tumour boundary. Thus, multiplying the magnitude squared *E*-field values increases the relative contribution to the SAR within the spherical tumour model.

Peak temperatures follow the trend of the SAR away from the skin surface, which is maintained at 39 °C by the circulating water bath. A water bath temperature above body temperature is afforded by the 140 MHz excitation frequency and the large aperture of the RF phased array applicator. This combination achieves heating within the breast without overheating the skin; therefore, skin cooling is not required for this system. In figure 8(c), a peak temperature of 42.5 °C is indicated within the tumour model. However, a larger peak temperature of 43.6 °C is encountered outside the tumour model in figure 9(c). Although the *E*-field is focused within the spherical tumour model and SAR results show that the peak SAR value in the tumour model is comparable to the peak SAR outside the tumour, the overall peak temperatures in the breast tumour model are nevertheless generated in fat. These results demonstrate that the boundary conditions, particularly the orientation of the *E*-field vector within the breast and tumour regions, strongly influence the resulting temperature distribution. Other results (not shown) demonstrate that the peak temperature increases in fat and decreases in the tumour as the focus moves away from the applicator and deeper into the tumour. This suggests that the penetration depth, combined with an impedance mismatch at the fat/tumour boundary, strongly influences the ability of RF devices to heat deep tumours in the breast. The results shown in figure 8 and figure 9 also suggest that both SAR and temperature calculations are required for these evaluations. The heat generated along the tumour boundary is expected to contribute to regional heating in the breast, increasing the temperature of arterial blood and thereby improving the temperature distribution in the tumour. This result also demonstrates the need for noninvasive magnetic resonance (MR) thermometry (Carter *et al* 1998) that provides valuable feedback for this regional heating device. Noninvasive thermometry will verify the temperature output generated by this RF phased array applicator, which is a function of the load that is presented to the applicator (i.e., for different patients). Temperature feedback will facilitate compensation for load changes and cross-coupling through phase and amplitude adjustments applied to the controlling amplifier outputs. This feedback will then improve targeted heating of breast tumours with this RF phased array device.

These results suggest that conformal heating of LABC tumours will be enhanced with an approach that incorporates an ultrasound (US) component within a hybrid RF/US phased array device. Measurement and simulation results show that the RF phased array is a regional heating device that heats a large portion of the intact breast, and adding local heat produced by an ultrasound phased array is expected to improve the temperature distribution in the distal portion of the tumour. The hybrid approach will exploit the regional heat generated by the RF applicator that increases the temperature of the arterial blood supply, and then the ultrasound component will locally raise the temperature as needed within the target volume. The existing RF phased array structure, which occupies four of the six flat panels in the Lexan structure, is ideal for incorporating additional ultrasound applicators. Furthermore, the large heated region created by the RF phased array combined with the small focal spots generated by the ultrasound phased array provides multiple opportunities for optimization of the temperature distribution produced by hybrid RF/US phased array devices. This RF phased array design, which fills four Lexan panels with end-loaded dipole antennas, is ideal for hybrid structures that incorporate additional ultrasound applicators into either of the remaining side panels. Other new geometries that populate all of the panels with end-loaded dipole antennas are also under development.

6. Conclusion

E-fields generated by a four-channel RF phased array applicator designed for hyperthermia cancer therapy in the intact breast were measured in a tank filled with deionized water. This geometry was simulated with the finite-element method, and the results indicate excellent agreement between the measured and simulated *E*-field magnitudes. The applicator generates a geometric focus at the centre of the water tank, and measurements and simulations show that, through the selection of appropriate phases and amplitudes applied to each of the antennas, this focus can also be steered off-axis. Some differences between the measured and simulated *E*-field magnitudes are evident in the geometric focus and the steered focus, and these are attributed to simulation errors and measurement errors. Overall, comparisons show that finite-element simulations successfully predict the focal pattern generated by the RF phased array applicator within the water tank.

Finite-element simulations were also evaluated in a simplified breast model that contains a spherical tumour volume. These simulations show that, although the RF phased array is focused within the spherical tumour model, the peak temperatures occur outside the tumour. These temperature peaks, which are a consequence of the material properties of fat and tumour and the orientation of the incident *E*-field, are immediately adjacent to the tumour, so these peaks enhance regional heating generated by the RF phased array applicator. The simulated *E*-field, SAR and temperature distributions suggest that this RF phased array applicator generates effective regional heat for hyperthermia treatments of locally advanced breast cancer. Future evaluations of this RF phased array applicator will include realistic 3D anatomy derived from CT and/or MR images.

References

Carter DL, MacFall JR, Clegg ST, Wan X, Prescott DM, Charles HC, Samulski TV. Magnetic resonance thermometry during hyperthermia for human high-grade sarcoma. Int. J. Radiat. Oncol. Biol. Phys 1998;40:815–822.

Clegg ST, Das SK, Fuller E, Anderson S, Blivin J, Oleson JR, Samulski TV. Hyperthermia treatment planning and temperature distribution reconstruction: a case study. Int. J. Hyperthermia 1996;12:65–76. [PubMed: 8676009]

Das SK, Clegg ST, Samulski TV. Electromagnetic thermal therapy power optimization for multiple source applicators. Int. J. Hyperthermia 1999a;15:291–308.

Das SK, Clegg ST, Samulski TV. Computational techniques for fast hyperthermia temperature optimization. Med. Phys 1999b;26:319–328.

Ebbini ES, Cain CA. Multiple-focus ultrasound phased-array pattern synthesis: optimal driving signal distributions for hyperthermia. IEEE Trans. Ultrason. Ferroelectr. Freq. Control 1989;36:540–548. [PubMed: 18290231]

Fenn AJ, Wolf GL, Fogle RM. An adaptive microwave phased array for targeted heating of deep tumours in intact breast: animal study results. Int. J. Hyperthermia 1999;15:45–61.

Fujita Y, Kato H, Ishida T. An RF concentrating method using inductive aperture-type applicators. IEEE Trans. Biomed. Eng 1993;40:110–113. [PubMed: 8468071]

Greenlee RT, Murray T, Bolden S, Wingo PA. Cancer statistics, 2000. CA-Cancer J. Clin 2000;50:7–33. [PubMed: 10735013]

Gromoll C, Lamprecht U, Hehr T, Buchgeister M, Bamberg M. An on-line phase measurement system for quality assurance of the bsd 2000: Part I. Technical description of the measurement system. Int. J. Hyperthermia 2000;16:365–373. [PubMed: 10949132]

Hildebrandt B, Wust P, Ahlers O, Dieing A, Sreenivasa G, Kerner T, Felix R, Riess H. The cellular and molecular basis of hyperthermia. Crit. Rev. Oncol. Hematol 2002;43:33–56. [PubMed: 12098606]

Hornsleth SN, Frydendal L, Mella O, Dahl O, Raskmark P. Quality assurance for radiofrequency regional hyperthermia. Int. J. Hyperthermia 1997;13:169–185. [PubMed: 9147144]

Hortobagyi GN. Comprehensive management of locally advanced breast cancer. Cancer 1990;66 (Suppl.):1387–1391.

Hynynen K, Pomeroy O, Smith DN, Huber PE, McDannold NJ, Kettenbach J, Baum J, Singer S, Jolesz FA. MR imaging-guided focused ultrasound surgery of fibroadenomas in the breast: a feasibility study. Radiology 2001;219:176–185. [PubMed: 11274554]

Jin, J. The Finite Element Method in Electromagnetics. New York: Wiley; 2002. p. 15

Joines WT, Zhang Y, Li C, Jirtle RL. The measured electrical properties of normal and malignant human tissues from 50 to 900 MHz. Med. Phys 1994;21:547–550. [PubMed: 8058021]

Kato H, Ishida T. Present and future-status of noninvasive selective deep heating using RF in hyperthermia. Med. Biol. Eng. Comput 1993;31:2–11. [PubMed: 8326759]

Kroeze H, Van de Kamer JB, De Leeuw AAC, Langendijk JJW. Regional hyperthermia applicator design using FDTD modelling. Phys. Med. Biol 2001;46:1919–1935. [PubMed: 11474934]

Kumaradas JC, Sherar MD. Edge-element based finite element analysis of microwave hyperthermia treatments for superficial tumours on the chest wall. Int. J. Hyperthermia 2003;19:414–430. [PubMed: 12850927]

Lamprecht U, Gromoll C, Hehr T, Buchgeister M, Bamberg M. An on-line phase measurement system for quality assurance of the BSD 2000: Part II. Results of the phase measurement system. Int. J. Hyperthermia 2000;16:365–373. [PubMed: 10949132]

Malinen M, Huttunen T, Hynynen K, Kaipio JP. Simulation study for thermal dose optimization in ultrasound surgery of the breast. Med. Phys 2004;31:1296–1307. [PubMed: 15191322]

Paulsen KD, Jia X, Sullivan JM Jr. Finite element computations of specific absorption rates in anatomically conforming full-body models for hyperthermia treatment analysis. IEEE Trans. Biomed. Eng 1993;40:933–945. [PubMed: 8288285]

Paulsen KD, Strohbehn JW, Hill SC, Lynch DR, Kennedy FE. Theoretical temperature profiles for concentric coil induction heating devices in a two-dimensional, axi-symmetric, inhomogeneous patient model. Int. J. Radiat. Oncol. Biol. Phys 1984;10:1095–1107. [PubMed: 6746351]

Paulsen KD, Strohbehn JW, Lynch DR. Theoretical electric field distributions produced by three types of regional hyperthermia devices in a three-dimensional homogeneous model of man. IEEE Trans. Biomed. Eng 1988;35:36–45. [PubMed: 3338810]

Perez CA, Graham ML, Taylor ME, Levy JF, Mortimer JE, Philpott GW, Kucik NA. Management of locally advanced-carcinoma of the breast: I. Noninflammatory. Cancer 1994;74 (Suppl.):453–465. [PubMed: 8004621]

Roemer RB, Cetas TC, Oleson JR, Halac S, Matloubieh AY. Comparative evaluation of hyperthermia heating modalities: I. Numerical analysis of thermal dosimetry bracketing cases. Radiat. Res 1984;100:450–472. [PubMed: 6505138]

Straube WL, Moros EG, Myerson RJ. Phase-stability of a clinical phased-array system for deep regional hyperthermia. Int. J. Hyperthermia 1995;11:87–93. [PubMed: 7714373]

Sullivan DM. Mathematical methods for treatment planning in deep regional hyperthermia. IEEE Trans. MTT 1992;39:864–872.

Sullivan DM, Borup DT, Gandhi OP. Use of the finite-difference time-domain method in calculating EM absorption in human tissues. IEEE Trans. Biomed. Eng 1987;34:148–157. [PubMed: 3557494]

Turner PF. Regional hyperthermia with an annular phased array. IEEE Trans. Biomed. Eng 1984;31:106–114. [PubMed: 6724597]

Turner PF. Mini-annular phased-array for limb hyperthermia. IEEE Trans. MTT 1986;34:508–513.

van der Zee J. Heating the patient: a promising approach? Ann. Oncol 2002;13:1173–1184. [PubMed: 12181239]

van Rhoon GC, van der Heuvel DJ, Ameziane A, Rietveld PJM, Volenec K, van der Zee J. Characterization of the SAR-distribution of the Sigma-60 applicator for regional hyperthermia using a Schottky diode sheet. Int. J. Hyperthermia 2003;19:642–654. [PubMed: 14756453]

Wiersma J, van Maarseveen RAM, van Dijk JDP. A flexible optimization tool for hyperthermia treatments with RF phased array systems. Int. J. Hyperthermia 2002;18:73–85. [PubMed: 11926190]

Wust P, Nadobny J, Felix R, Deuflhard P, Louis A, John W. Strategies for optimized application of annular-phased-array systems in clinical hyperthermia. Int. J. Hyperthermia 1991;7:157–173. [PubMed: 2051070]

Wust P, Hildebrandt B, Sreenivasa G, Rau B, Gellermann J, Riess H, Felix R, Schlag PM. Hyperthermia in combined treatment of cancer. Lancet Oncol 2002;3:487–497. [PubMed: 12147435]

Zhang Y, Joines WT, Jirtle RL, Samulski TV. Theoretical and measured electric field distributions within an annular phased array: consideration of source antennas. IEEE Trans. Biomed. Eng 1993;40:780–787. [PubMed: 8258444]
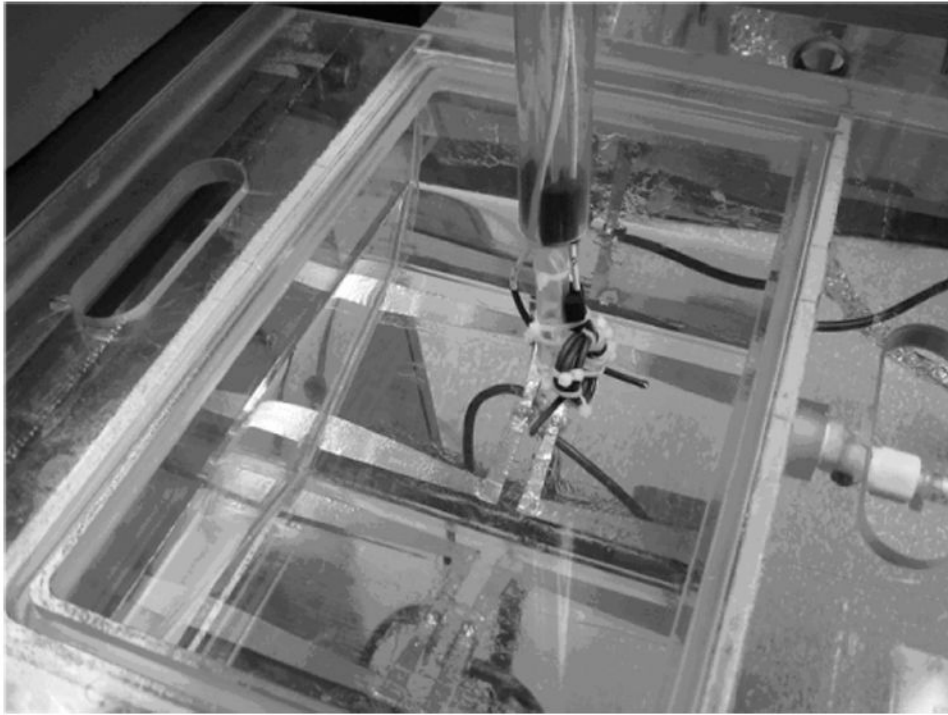
Figure 1.
Four-antenna RF phased array prototype designed for hyperthermia treatments in the intact breast.
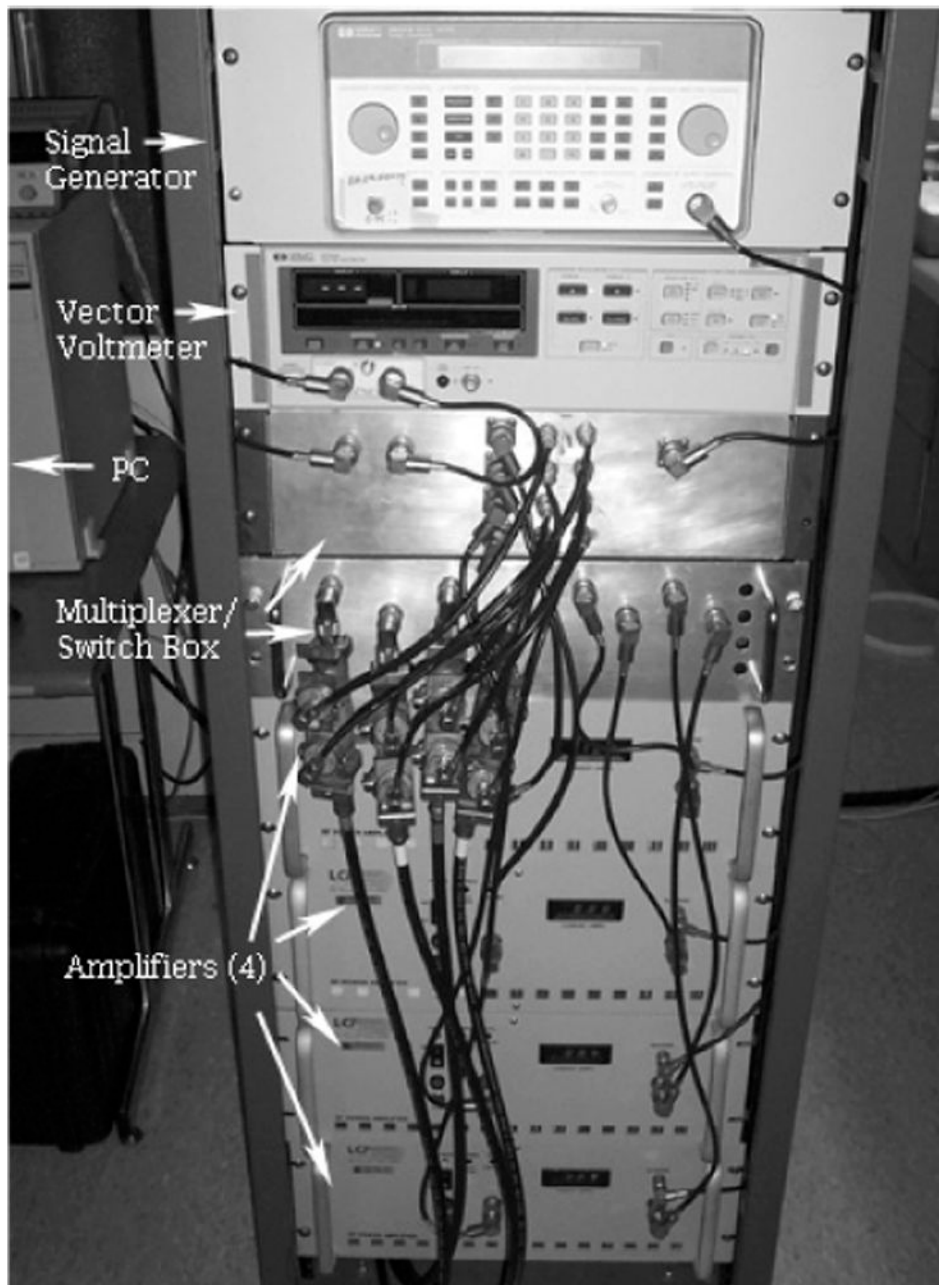
Figure 2.
RF phased array amplifier system. This rack-mounted system consists of a signal generator, a vector voltmeter, a multiplexer/switch box and four RF power amplifiers. The signal source generates a common excitation frequency for each of the amplifiers, the vector voltmeter provides phase and power feedback, and the multiplexer/switch box combination controls the inputs to the RF amplifiers. In turn, the RF amplifiers drive the individual antennas in the phased array applicator.
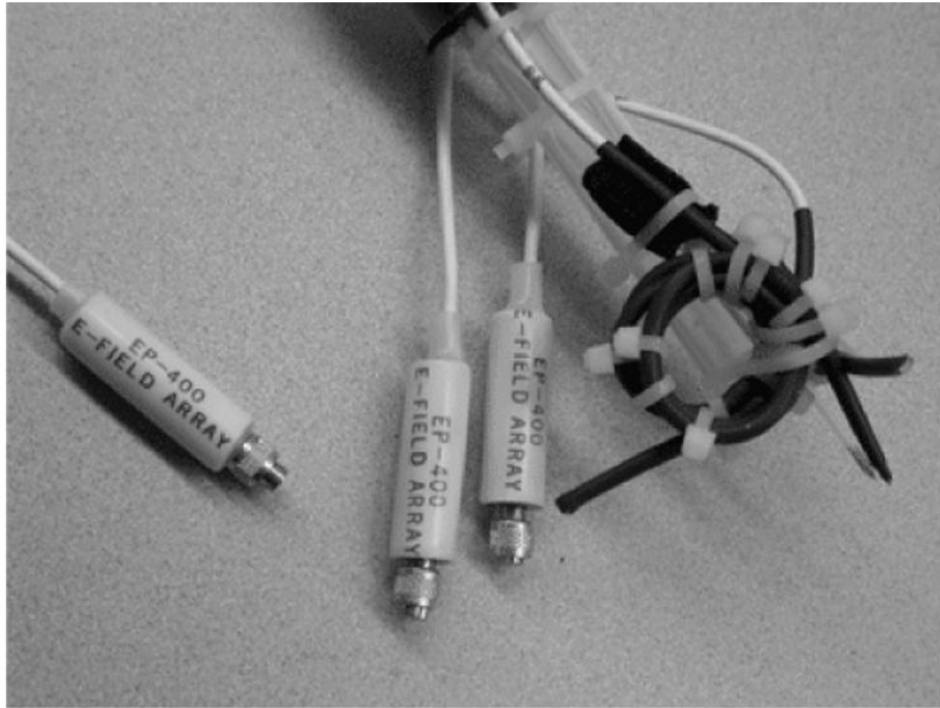
Figure 3.
Three *E*-field array probes are attached to a Plexiglas rod for measurements of the electric field produced by the RF applicator. This probe arrangement is scanned across a rectilinear grid within the water tank by a computer-controlled positioning system. The measurements obtained with these scans characterize the *E*-field distribution generated by the RF phased array.
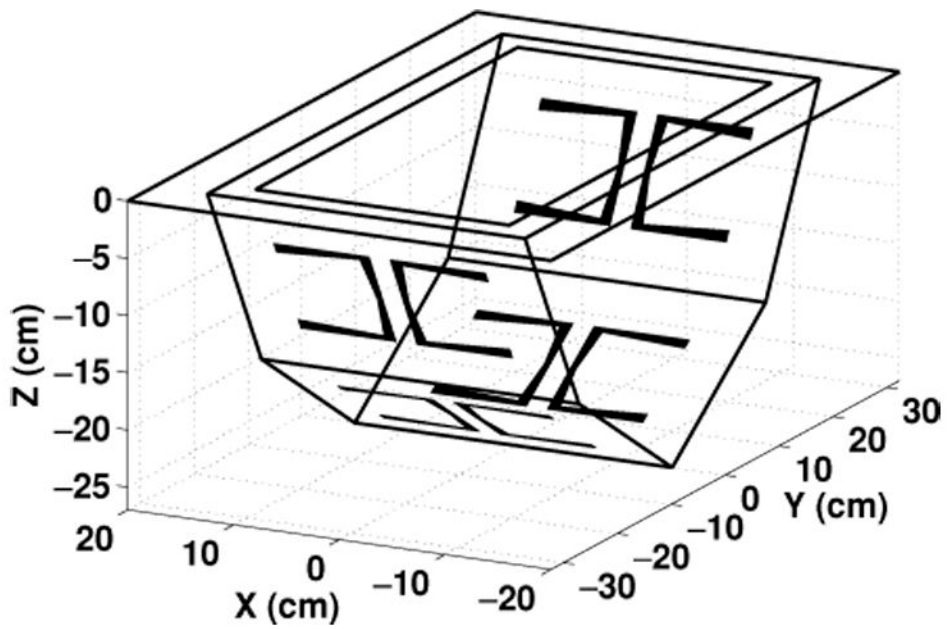
Figure 4.
Simulation model for the four-antenna RF phased array applicator. The geometric model, which has the same dimensions as the applicator in figure 1, defines the input parameters for finite-element simulations.
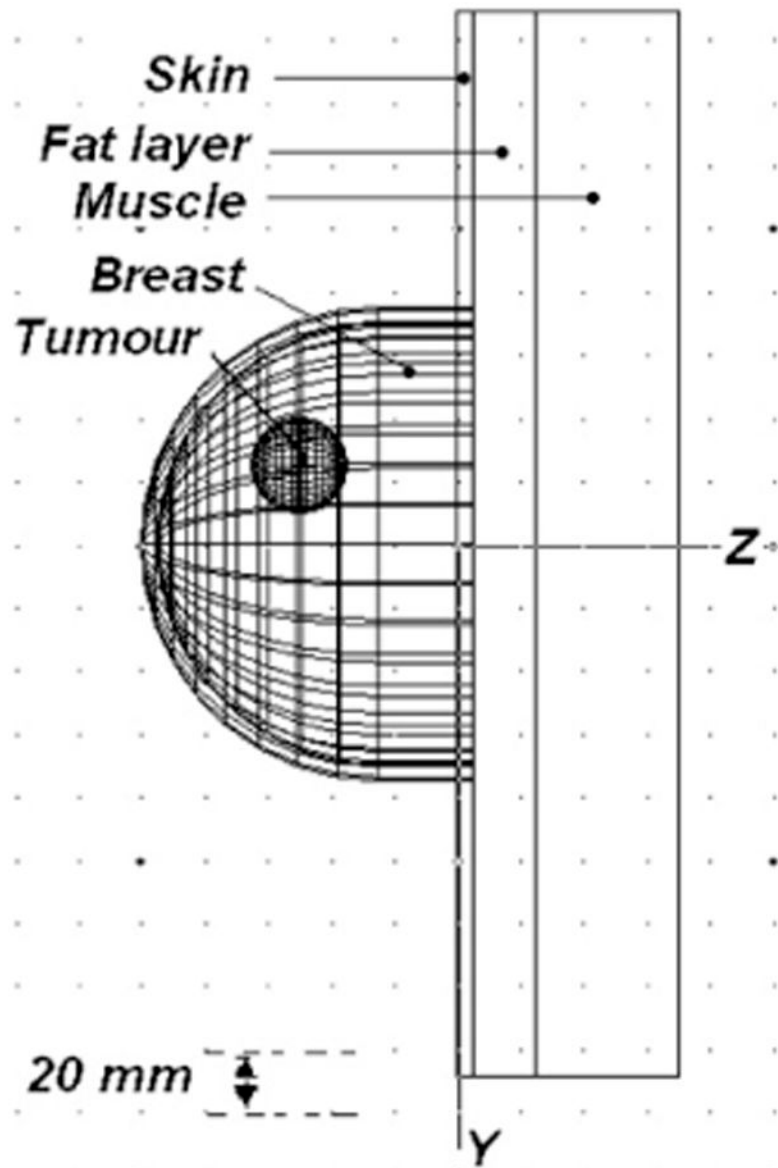
Figure 5.
Schematic of the breast model defined for FEM simulations. The breast is modelled by a hemisphere with a 75 mm radius, and a spherical tumour model with a 25 mm radius is located inside the breast. The hemispherical breast model is attached to a 5 mm thick skin layer, a 25 mm thick fat layer and a 42 mm thick muscle layer.
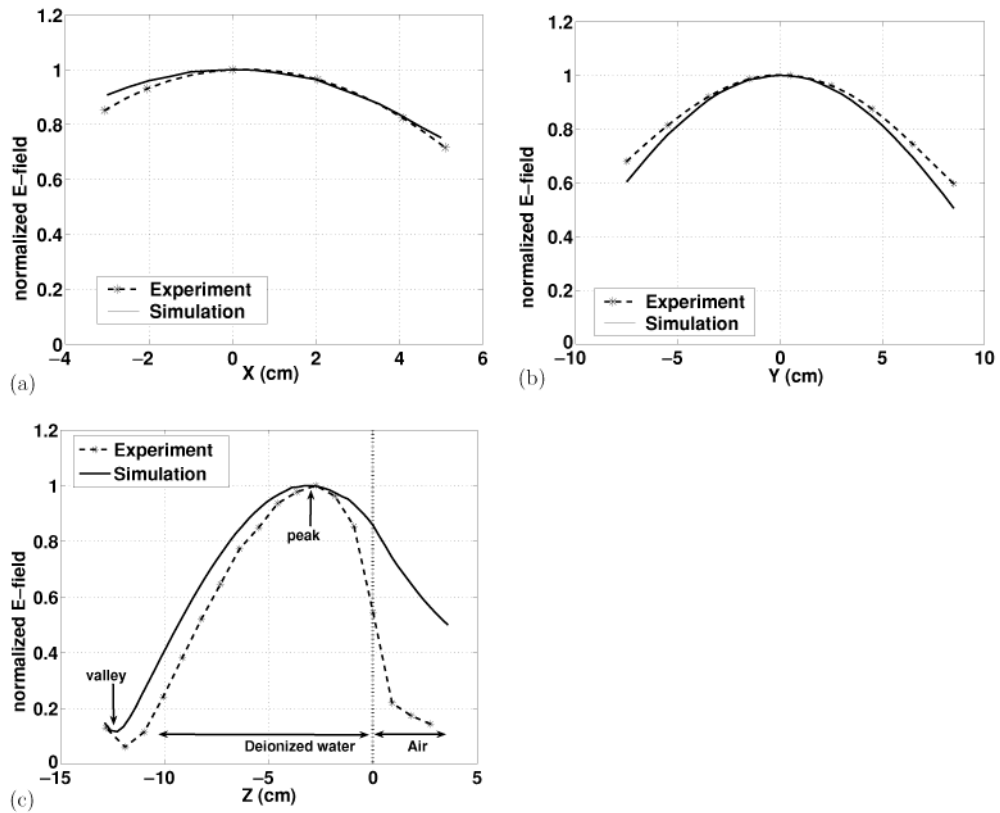
Figure 6.
E-field distributions generated by the RF phased array depicted in figure 1. The applicator prototype operates at 140 MHz, producing a focus at the centre of a tank filled with deionized water. The *E*-field measurements are performed by the apparatus depicted in figure 3, and the *E*-field is computed with the finite-element method for uniform phase and amplitude inputs. The finite-element simulations successfully reproduce the total measured *E*-field in all three directions. Measured (dashed line) and simulated (solid line) *E*-field values in the water tank are plotted with respect to (a) the *x* coordinate where $y = 0$ and $z = -3$ cm, (b) the *y* coordinate where $x = 0$ and $z = -3$ cm, and (c) the *z* coordinate where $x = 0$ and $y = 0$ cm. In particular, (c) shows that the finite-element calculations predict the locations of the maximum and minimum *E*-field magnitudes along the *z*-axis.
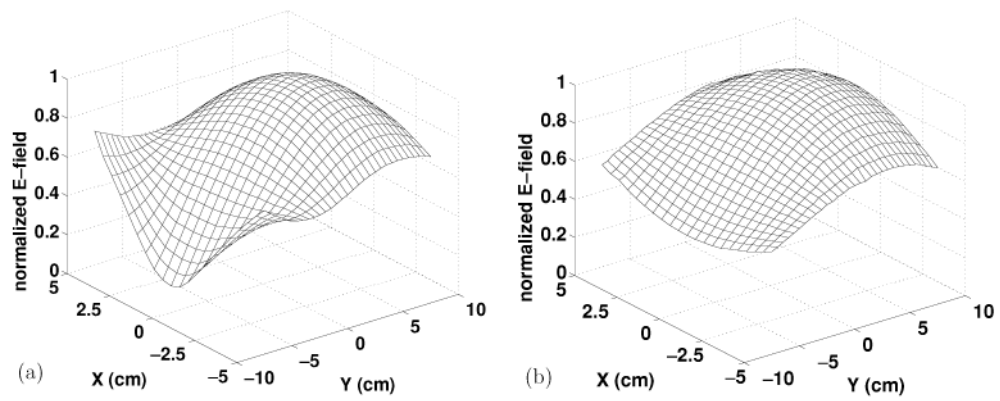
Figure 7.
Examples of measured (a) and simulated (b) 140 MHz *E*-fields in the *xy* plane achieved through electronic steering. Although some differences appear near the far corners of the grid, the shapes of these *E*-field meshes are quite similar, particularly in the region near the peak. In (a) and (b), the *E*-field is measured 3 cm below the water surface ($z = -3$ cm).
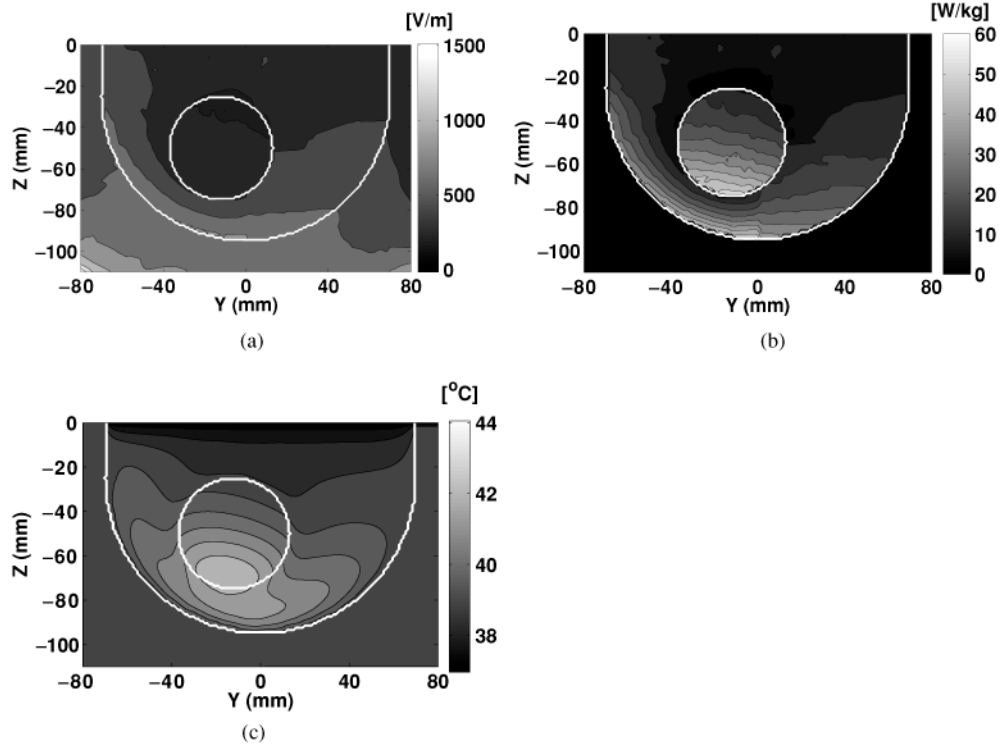
Figure 8.
Simulated (a) *E*-field, (b) SAR and (c) temperature distributions generated by the RF phased array applicator and evaluated in the *x* = 0 plane of the breast tumour model, where the white contours indicate the external outlines of the breast and tumour. These simulation results show that, in the *x* = 0 plane, the *E*-field peaks in water are near the source antennas, the *E*-field peaks in tissue are near the skin surface, the peak SAR values are within the tumour model and near the skin surface, and the peak temperature in the *x* = 0 plane (the peak temperature in this plane is 42.5 °C) is within the tumour boundary.
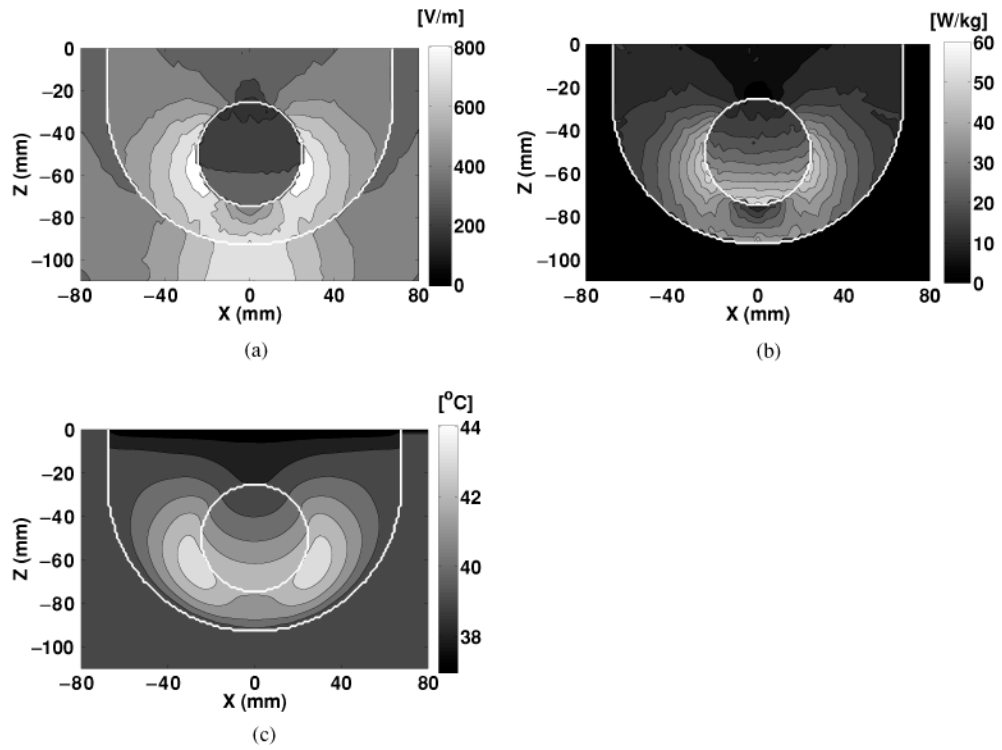
Figure 9.
Simulated (a) *E*-field, (b) SAR and (c) temperature distributions generated by the RF phased array applicator and evaluated in the $y = -16$ mm plane of the breast tumour model. In the $y = -16$ mm plane, *E*-field peaks in tissue appear in fat near the tumour interface, peak SAR values are in fat near the tumour interface and in the tumour proximal to the applicator, and the peak temperature in the $y = 0$ plane is located in fat near the tumour interface. The peak temperature in this figure, which is also the peak overall temperature, is 43.6 °C.

Table 1.

Material properties for the breast model in figure 5. The values of ε_r and σ are from Joines *et al* (1994) and the values of c_p, κ and W are from Kroeze *et al* (2001).

	Fat	Muscle	Tumour
Relative permittivity ε_r	20.4	75	65
Electrical conductivity σ (S m^{-1})	0.12	0.75	0.78
Specific heat c_p (J kg^{-1} °C^{-1})	2387	3639	3639
Thermal conductivity κ (W m^{-1} °C^{-1})	0.22	0.56	0.56
Blood perfusion W (kg m^{-3} s^{-1})	1.1	3.6	1.8